Sensitivity of Tropical Wave Structure to Resolution and Convection Treatment in a Global Non-Hydrostatic Model

Falko JUDT and Rosimar RIOS-BERRIOS

NSF National Center for Atmospheric Research, Colorado, USA

Abstract

Tropical waves shape weather across equatorial regions, yet their representation in global models remains a formidable challenge. This study investigates how model fidelity depends on two key factors: horizontal resolution (120 km to 3.75 km) and the treatment of convection (parameterized vs. explicit). The 3.75-km simulation with explicit convection most faithfully reproduces wave structures and wave-driven rainfall. Interestingly, a 15-km simulation with an alternative parameterization scheme achieves comparable structural fidelity and wave-driven rainfall, but at the cost of a pronounced overall precipitation bias. Moreover, simulations that excel at capturing wave structure tend to perform poorly in reproducing propagation speed, whereas parameterized simulations—though less realistic in structure and rainfall—represent speed more accurately. This trade-off highlights both the promise and the limitations of global kilometer-scale models and underscores the need for continued model development to advance tropical weather and climate prediction.

Citation   Judt, F., and R. Rios-Berrios, 2025: Sensitivity of tropical wave structure to resolution and convection treatment in a global non-hydrostatic model. *J. Meteor. Soc. Japan*, **103**, 000–000, doi:10.2151/jmsj.2025-036.

1.   Introduction

Tropical waves are fundamental drivers of weather in the tropics. They modulate rainfall patterns, trigger heavy precipitation events, and contribute to tropical cyclone formation. The accurate representation of these waves in numerical models is therefore essential for improving forecasts across all timescales. To systematically evaluate how horizontal resolution and convection treatment affect the simulation of tropical waves, we analyze their three-dimensional structure in a hierarchy of global simulations. Our experiments use mesh spacings of 120, 15, and 3.75 km—representing conventional climate models, operational numerical weather prediction systems, and emerging kilometer-scale models, respectively. This approach builds on recent work suggesting that explicit convection at fine resolutions improves wave fidelity (Weber et al. 2020, 2021; Judt and Rios-Berrios 2021; Rios-Berrios et al. 2023).

1.1   Background and motivation

Despite significant advances in global modeling, the faithful representation of tropical waves remains a persistent challenge. This deficiency degrades tropical weather forecasts (Dias et al. 2018; Vogel et al. 2018, 2020) and compromises the realistic simulation of tropical climate variability (Lin et al. 2006, 2008; Straub et al. 2010; Bartana et al. 2023). The resulting

Corresponding author: Falko Judt, NSF National Center for Atmospheric Research, P.O. Box 3000, Boulder, CO 80307, USA
E-mail: fjudt@ucar.edu

uncertainty is evident in substantial discrepancies among different models (Lin et al. 2006; Nakajima et al. 2013; Bartana et al. 2023; Lee et al. 2025) and even reanalysis datasets (Chien and Kim 2023). The source of this widespread disagreement is largely attributed to the sensitivity of models to their cumulus parameterization schemes (Bengtsson et al. 2019; Zhu et al. 2020; Lee et al. 2025), wherein even subtle variations in a single scheme's formulation or parameters can yield vastly different simulation outcomes (Frierson et al. 2011).

The sensitivity to cumulus parameterization undermines confidence in model predictions and has motivated the exploration of alternative approaches. Insights from mesoscale meteorology have long suggested that explicitly resolving convection, rather than parameterizing it, provides a more physically robust foundation for simulating convectively driven phenomena. The promise of this approach for tropical waves was long thwarted by a significant practical barrier: the prohibitive computational cost of achieving convection-permitting resolutions (typically below 5 km) on a global scale.

With sustained advancements in high-performance computing, such simulations eventually became feasible. Pioneering work by Japanese researchers in the mid-2000s demonstrated the potential of global models capable of explicitly simulating convection (Tomita et al. 2005; Miura et al. 2007; Satoh et al. 2008; Fudeyasu et al. 2008). As computational power and expertise grew, atmospheric research centers worldwide began adopting these global km-scale models[1], culminating in collaborative initiatives like the DYnamics of the Atmospheric general circulation Modeled On Non-hydrostatic Domains (DYAMOND) project (Stevens et al. 2019). Findings from these efforts have consistently shown that global km-scale models enhance the fidelity of simulated atmospheric processes compared to their lower-resolution counterparts.

An emerging advantage of global km-scale models is their improved simulation of tropical weather phenomena such as the Madden-Julian Oscillation and tropical cyclones (Miyakawa et al. 2014; Kodama et al. 2015; Judt et al. 2021). A recent trio of studies used the Model for Prediction Across Scales–Atmosphere (MPAS–A) to investigate the influence of grid spacing and convection treatment on tropical waves (Judt and Rios-Berrios 2021; Weber et al. 2021; Rios-Berrios et al. 2023). Collectively, this body of work shows

that simulations with explicit deep convection more accurately capture tropical waves—particularly those of the gravity-wave type—while simulations relying on parameterized convection struggle to reproduce these waves and, in particular, their heating profiles.

While foundational, those studies have key limitations that constrain the generality of their findings. The idealized aquaplanet configuration in Rios-Berrios et al. (2023), for instance, complicates validation against real-world observations, while the narrow focus on rainfall in (Judt and Rios-Berrios 2021) leaves the broader kinematic and thermodynamic wave structures unexamined. The present study bridges these gaps by performing a comprehensive, multi-variable structural analysis on the same realistic, real-data simulations used by Judt and Rios-Berrios (2021), thereby providing a more complete assessment of model performance.

The remainder of this paper is organized as follows: Section 2 describes the simulations, observations, and analysis methods. Section 3 provides an initial assessment of precipitation and waves, followed by a detailed comparison of horizontal and vertical wave structures and phase speed in Section 4. We discuss the implications of our findings in Section 5 and summarize our conclusions in Section 6.

2.   Data and methods

2.1   Simulations

The present study is based on six simulations produced with the MPAS-A global nonhydrostatic model (Skamarock et al. 2012), configured as described in Judt et al. (2021). The experimental setup follows the DYAMOND protocol (Stevens et al. 2019): all runs were initialized at 0000 UTC 1 August 2016 and integrated for 40 days. Data for the initial conditions, as well as for the prescribed sea surface temperatures and sea ice, were obtained from the European Centre for Medium-Range Weather Forecasts (ECMWF).

The six simulations comprise two distinct sets (Table 1). The first is a subset of the resolution ensemble from Judt and Rios-Berrios (2021), featuring the scale-aware Tiedtke cumulus scheme (Wang 2022) across three mesh spacings:

- At 3.75 km, convection is largely resolved explicitly, with the parameterization contributing only 12 % of total precipitation. This run is therefore designated 3.75-km EXP.
- At 15 km and 120 km, parameterized convection dominates ($>$ 95 % of precipitation), and the runs are designated 15-km PAR and 120-km PAR, respectively.

---

[1] Also referred to as global storm-resolving models or global convection-permitting models.

Table 1. Summary of simulations. The three nominal simulations are listed first, followed by the sensitivity runs. The table includes each simulation's label, cumulus parameterization scheme, and the dominant convection representation.

Simulation	Parameterization Scheme	Convection Representation
3.75 km EXP	Scale-aware Tiedtke	Mostly explicit (12 % parameterized)
15 km PAR	Scale-aware Tiedtke	Mostly parameterized (96 %)
120 km PAR	Scale-aware Tiedtke	Mostly parameterized (97 %)
3.75 km PAR	Tiedtke	Mostly parameterized (89 %)
15 km EXP	None	Fully explicit (0 % parameterized)
15 km PAR-2	Old Tiedtke	Mixed (59 % parameterized)

The second set is a sensitivity ensemble of three supplementary simulations designed to isolate the impact of different convection treatments:

1. 3.75-km PAR: A high-resolution run that, unlike its nominal counterpart, uses the non-scale-aware Tiedtke scheme (Zhang and Wang 2017) to assess the impact of a full cumulus parameterization at convection-permitting resolution.

2. 15-km EXP: A simulation at 15-km resolution in which the cumulus parameterization is disabled entirely, forcing the model to explicitly resolve convection at a moderately coarse mesh spacing.

3. 15-km PAR-2: A 15-km run that uses an earlier version of the non-scale-aware Tiedtke scheme to explore sensitivity to the parameterization's formulation.

The model output was interpolated to a 0.25° latitude-longitude grid to match the resolution of the observational datasets described in the following subsection and to facilitate comparisons across simulations. Conservative interpolation ensures that the global mean of each field is the same before and after interpolation. This was accomplished using the Climate Data Operators (Schulzweida 2023).

2.2 Observations

To assess how well the simulations capture tropical waves, we used two observation-based datasets:

- NASA's Integrated Multi-SatellitE Retrievals for Global Precipitation Measurement (IMERG; Huffman et al. 2020): This dataset combines rainfall data from multiple satellites into a gridded format with 0.1° latitude × longitude resolution. For this study, we adopted the 30-minute IMERG final product, conservatively interpolated to six-hourly rates on a 0.25° grid.

- ECMWF Reanalysis 5th Generation (ERA5; Hersbach et al. 2020): We utilized atmospheric fields from ERA5 to provide a consistent comparison against the simulated fields.

We acknowledge that these datasets, particularly the reanalysis, are model-based and therefore not true observations in a strict sense.

2.3 Wave identification and composite technique

We employed a phase composite technique, adapted from Rios-Berrios et al. (2023), with the following steps to isolate the wave signals in both observations and simulations:

1. Averaging and Filtering of rainfall fields:
   - Averaging: Six-hourly rainfall rates were averaged within the 5−15°N latitude band.
   - Filtering: The resulting time-longitude arrays underwent spatiotemporal filtering using the method developed by Wheeler and Kiladis (1999). Following Judt and Rios-Berrios (2021), we focused on the following tropical wave types:
     - Kelvin Waves: Eastward-propagating disturbances with wavenumbers 1−14 and periods of 2.5 days to 20 days.
     - $n = 1$ Inertio-Gravity Waves: Westward-propagating disturbances with wavenumbers 1−14 and periods of 1.8 days to 4.5 days.
     - Easterly Waves: Westward-propagating disturbances with wavenumbers 6−28 and periods of 2.5 days to 7.0 days.

2. Normalization, Phase-space Assignment, and Compositing:
   - Normalization: The filtered rainfall rates and their time derivatives were normalized by their standard deviations at each longitude.
   - Phase Space Assignment: Normalized values were assigned to a phase space, mapping each longitude-time coordinate to a corresponding wave phase.
   - Phase Binning: The wave phase was divided into 16 bins across eight phases, with Phase 5 representing the convectively active phase and Phase 1 representing the suppressed phase.
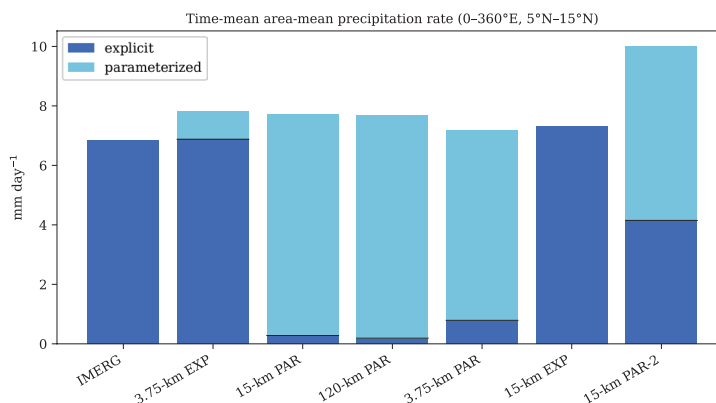   - Compositing: After binning, data points in each

Fig. 1.   Time-mean area-mean precipitation rate, averaged over 1 August–10 September 2016 and the region [0–360°E, 5–15°N], from IMERG and the six MPAS simulations. Contributions from the microphysics scheme ("explicit") are shown in dark blue, while contributions from the parameterization scheme ("parameterized") are shown in light blue.

phase were averaged.

3. Anomaly Calculation:

- Anomaly Calculation: Anomalies were calculated relative to the time and zonal mean for both observed and simulated fields. Unlike Rios-Berrios et al. (2023), we did not remove the annual and seasonal cycles from the ERA5 and IMERG datasets due to the shorter simulation period.

2.4   Phase speed analysis

Following the filtering process described in the previous subsection, we isolated strong waves by screening for where the wave signal exceeded one standard deviation above its temporal mean. We then identified the crests of the strong waves and created wave tracks by connecting these points in the longitude-time domain. Only wave tracks that lasted at least two days were included in the final analysis. For each track, we calculated the phase speed using the centered difference method (dx/dt). These phase speeds were then grouped into frequency distributions for visualization.

3.   Initial assessment of precipitation and wave-induced rainfall anomalies

We first present bulk precipitation metrics as a first assessment of model fidelity. Most simulations produce time- and area-averaged rainfall rates close to the observed IMERG value of 7 mm day^{-1}, though with a slight tendency toward overestimation (Fig. 1). The 15-km PAR-2 simulation is a clear outlier with a significant wet bias, producing nearly 10 mm day^{-1}. This run is also unique in its precipitation partitioning, with explicit and parameterized precipitation contributing

40 % and 60 %, respectively. In contrast, the other simulations are dominated by a single precipitation source: rainfall in the 3.75-km and 15-km EXP runs is primarily or entirely explicit, while the PAR runs produce overwhelmingly parameterized precipitation.

A comparison of the 40-day mean rainfall distributions reveals that the 3.75-km EXP run provides the closest match to observations, successfully capturing the fine-scale structure and localized maxima (Figs. 2a, b). This contrasts sharply with the parameterized convection (PAR) runs, which are all characterized by overly smooth fields and a spurious band of heavy rainfall across the monsoon regions of Southeast Asia and the western Pacific (Figs. 2c–e). The 15-km sensitivity experiments introduce other distinct flaws. The 15-km EXP run suffers from pixelated artifacts and fails to capture key monsoon rainfall maxima (Fig. 2f). The 15-km PAR-2 run exhibits its characteristic wet bias as a widespread positive anomaly and produces a unique rainfall pattern east of 120°E, with a pronounced southward shift in peak precipitation (Fig. 2g).

To analyze rainfall variability and propagating features, we use Hovmöller diagrams (Fig. 3). The IMERG data reveal a mix of eastward- and westward-propagating signals, reflecting the dynamic alternation of wet and dry periods across time and space (Fig. 3a). Among the simulations, the 3.75-km EXP run again provides the closest visual match to observations, capturing both the propagation and modulation of rainfall features (Fig. 3b). Interestingly, the 15-km PAR-2 run also captures propagating structures, but its fidelity is obscured by the pervasive wet bias (Fig. 3g).
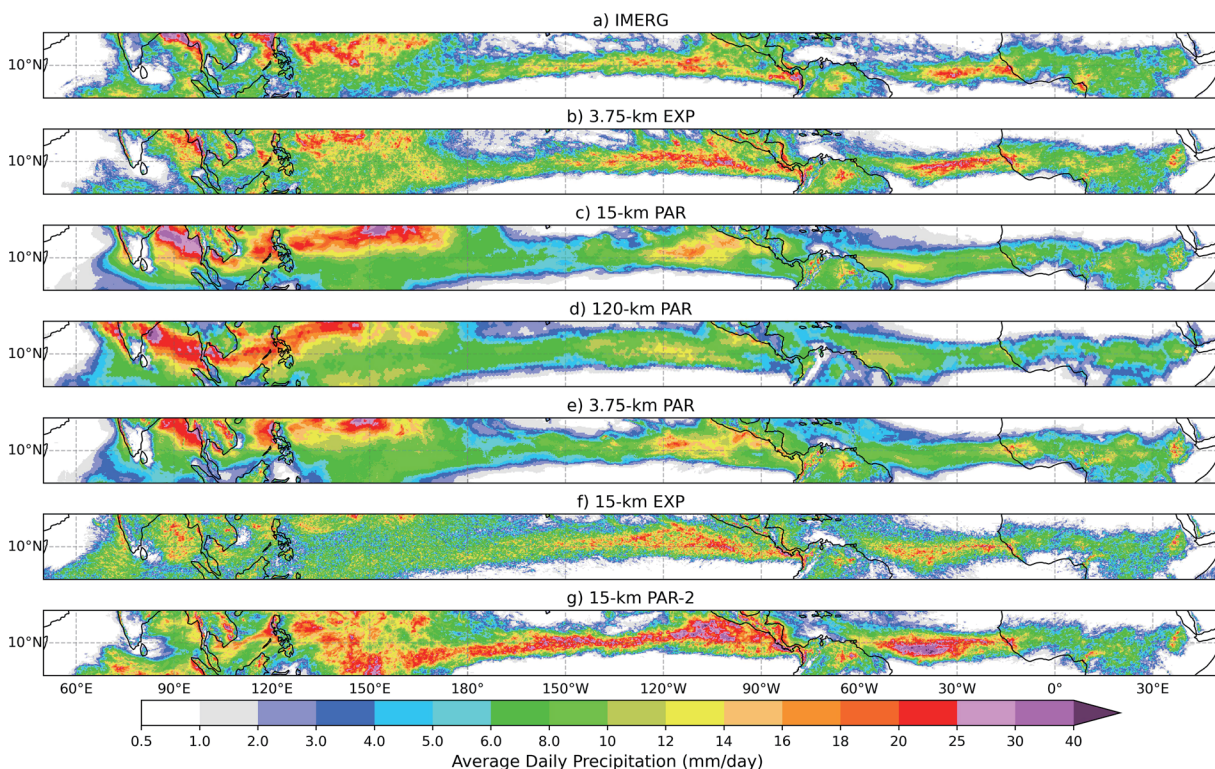
Fig. 2. Time-mean precipitation rate averaged over the period 1 August–10 September 2016, shown for (a) IMERG and (b–g) the six MPAS simulations.

The other simulations exhibit more pronounced structural deficiencies. The 15-km and 120-km PAR runs show limited contrast between active and suppressed rainfall. More specifically, precipitation is generally lighter but distributed over a much larger area. These overly expansive regions of light to moderate rain are almost certainly a manifestation of the "raining too often but far too lightly" problem that plagues models with parameterized convection (e.g., Stephens et al. 2010, see also Fig. 3 in Judt et al. 2021 for probability density functions of rainfall rate). This issue coincides with weak or absent propagating signals. Both simulations also produce a spurious, stationary rainfall maximum over the Indo-Pacific warm pool (90–180°E; Figs. 3c, d)—a feature likely tied to the artificial monsoonal rain band seen in Figs. 2c, d. Since these runs rely primarily on parameterized precipitation, the issue may stem from the convection scheme. However, the absence of this maximum in the 3.75-km PAR run (Fig. 3e) suggests that parameterization alone does not fully account for it. Despite using explicit convection, the 15-km EXP run is also deficient, exhibiting a grainy, disorganized precipitation

pattern that lacks key rainfall maxima and propagating signals between 90° and 180°E (Fig. 3f). Together, these results highlight the limitations of both coarse resolution and parameterized convection in accurately simulating the spatio-temporal variability of tropical rainfall.

To isolate the rainfall directly associated with wave activity, we analyze composite rainfall anomalies for each wave type (Fig. 4). In IMERG, these anomalies form a distinct sinusoidal pattern, with an active phase centered on wave phase 5 and a suppressed (negative) phase centered on wave phase 1. The amplitude varies by wave type: Easterly waves are strongest (0.25 mm h^{-1}), while Kelvin and inertio-gravity waves are weaker (approximately 0.15 mm h^{-1}). As for the simulations, the 3.75-km EXP run most faithfully reproduces the observed rainfall anomalies across all wave types. The 15-km PAR-2 run also performs well, emerging as a clear second. The fully explicit 15-km EXP run ranks third, underestimating the amplitudes of Kelvin and inertio-gravity waves, though it captures easterly waves somewhat more effectively. The remaining PAR simulations (3.75-, 15-, and 120-km)
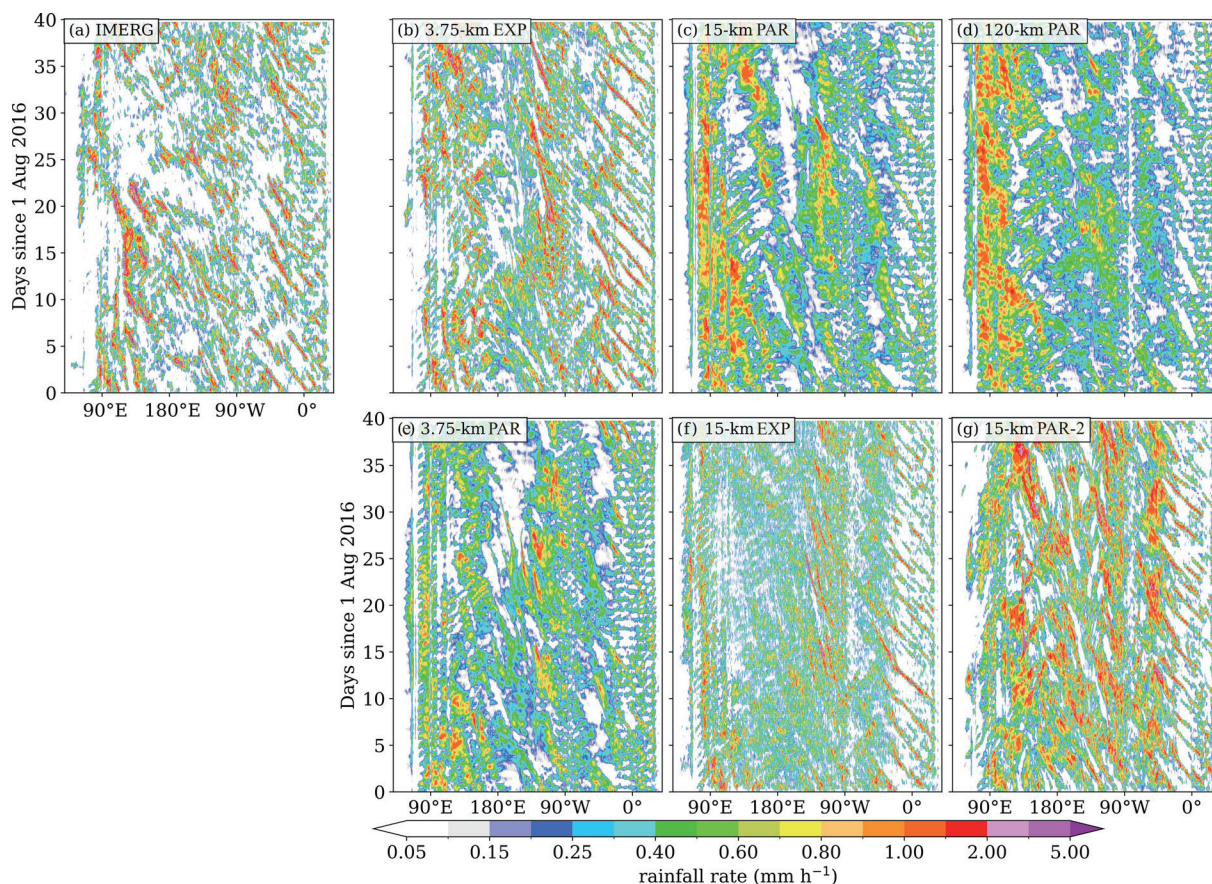
Fig. 3.   Hovmöller diagrams of 5–15°N latitudinally averaged precipitation from 1 August–10 September 2016. (a) IMERG; (b)–(d) nominal MPAS simulations with cell spacings indicated at the top of each panel; (f)–(h) sensitivity simulations (details in the text).

exhibit a shared deficiency and underestimate observed rainfall amplitudes by approximately 50 %. Building on these findings, the next section examines whether the ability to represent rainfall amplitude translates into skill in capturing the waves' underlying dynamical structures.

4.   Analysis of wave structure and phase speed

We assess each wave's horizontal structure using composites of rainfall and cloud water anomalies (overlaid with low- and upper-level winds, respectively) and its vertical structure using composites of vertical velocity, divergence, humidity, and temperature/heating fields.

4.1   Kelvin waves
a.   Horizontal structure

Observations reveal a Kelvin wave–induced rain and cloud anomaly spanning 5–15°N, concentrated between wave phases 4 and 6. The associated low-level winds exhibit a classic Kelvin wave structure: westerly anomalies, located within and to the west of the precipitation shield, converge with easterly anomalies to its east along a confluence zone in wave phase 6. A corresponding diffluence zone appears in phase 2. In the upper troposphere, the flow is roughly in quadrature with the lower levels, shifting the diffluence zone to the western edge of the cloud shield near phase 4, and the confluence zone to phases 7 and 8.

While all simulations capture the Kelvin wave signals, they do so with varying degrees of realism. The amplitude of the simulated rain and cloud anomalies mirrors the anomalies presented in Fig. 4. Specifically, the 3.75-km EXP and 15-km PAR-2 runs produce the strongest and, from a magnitude perspective, most realistic precipitation signals (Figs. 5b, g). In contrast, the other simulations show weaker or distorted rainfall patterns (Figs. 5c–f).
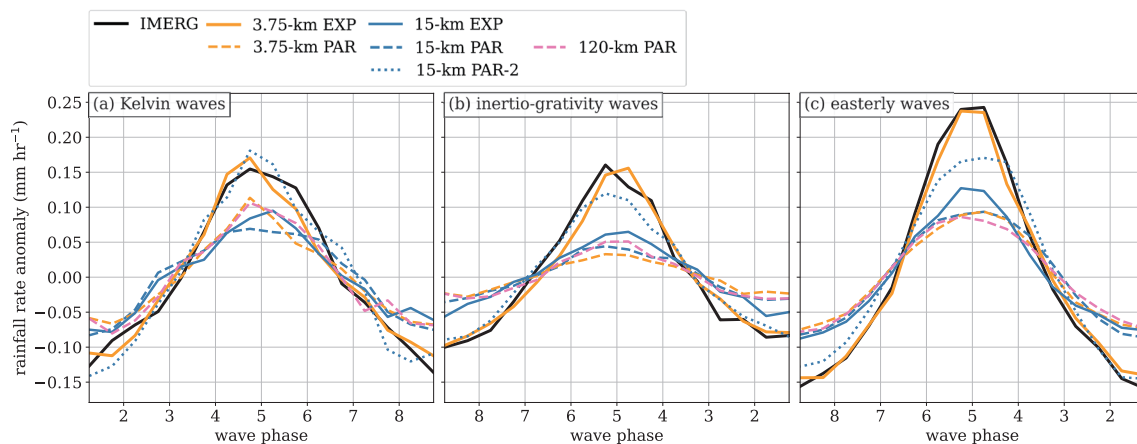
Fig. 4. Rainfall rate anomalies induced by (a) Kelvin waves, (b) inertio-gravity waves, and (c) easterly waves. IMERG "observations" are shown in black. Solid lines represent simulations where the overwhelming amount of precipitation is explicit, dashed lines indicate runs where most of the precipitation is parameterized, and dotted lines correspond to the 15-km PAR-2 run (which has nearly an equal split between explicit and parameterized precipitation). The 3.75-km runs are shown in orange, the 15-km runs in dark blue, and the 120-km run in pink.

Beyond anomaly strength, a key differentiator is the realism of the phase relationship between the wind and rainfall fields. This structural accuracy is determined by the model's treatment of convection. Simulations with explicit convection accurately capture the observed structure; they correctly place low-level confluence at the leading edge of the rain shield (Figs. 5b, f) and upper-level diffluence at the trailing edge of the cloud shield (Figs. 5i, m). In contrast, runs using parameterized convection misalignments. In the lower levels, the confluence is misplaced too far into the rain shield in the 15-km PAR and PAR-2 runs (Figs. 5c, g), or shifted too far ahead of it in the 3.75-km PAR run (Fig. 5e). Similar errors occur in the upper levels, where the diffluence is incorrectly positioned within the cloud shield in the 120-km PAR and 15-km PAR-2 runs, rather than at its rear edge (Figs. 5k, n). The 3.75-km PAR run displays a particularly unrealistic structure, with strong upper-level easterlies blanketing the entire cloud shield (Fig. 5l).

b. Vertical structure

The observed vertical structure of Kelvin waves is characterized by a "boomerang" shape, which arises from a westward tilt from the surface into the upper troposphere that reverses to an eastward tilt at the highest levels (Figs. 6a, h, o). This shape is exemplified by the wave's vertical motion, where ascent tilts westward with height up to around 200 hPa before weakening and tilting eastward at higher levels (Fig.

6a). Ascent is coupled with a divergence field that also tilts westward, forming a pronounced vertical dipole: low-level convergence is strongest near the surface in phase 6, while upper-level divergence peaks at 200 hPa between phases 4 and 5, above the core of strongest ascent.

The moisture and thermal fields display a similar boomerang shape. The moisture composite tilts westward up to 400 hPa and eastward above (Fig. 6h). While the mixing ratio and relative humidity fields share this overall shape, their peaks occur at different altitudes: the mixing ratio anomaly is greatest near 800 hPa, whereas the relative humidity anomaly is highest around 300 hPa.

The thermal structure mirrors the moisture pattern, although its characteristic "elbow" is found higher, near 300 hPa, with warm anomalies tilting westward through the troposphere with peaks at three distinct levels: near the surface, 600 hPa, and 250 hPa (Fig. 6o). The apparent heat source[2] displays a similar tilt but leads the temperature field in phase, which is consistent with diabatic heating acting as the primary driver of the temperature anomaly.

Overall, the simulations reproduce the Kelvin wave's tilted vertical structure, but with varying am-

---

[2] The apparent heat source (Q1) is the residual of the dry static energy equation (Yanai et al. 1973) and serves as a proxy for diabatic heating, which is not directly available from the model output.
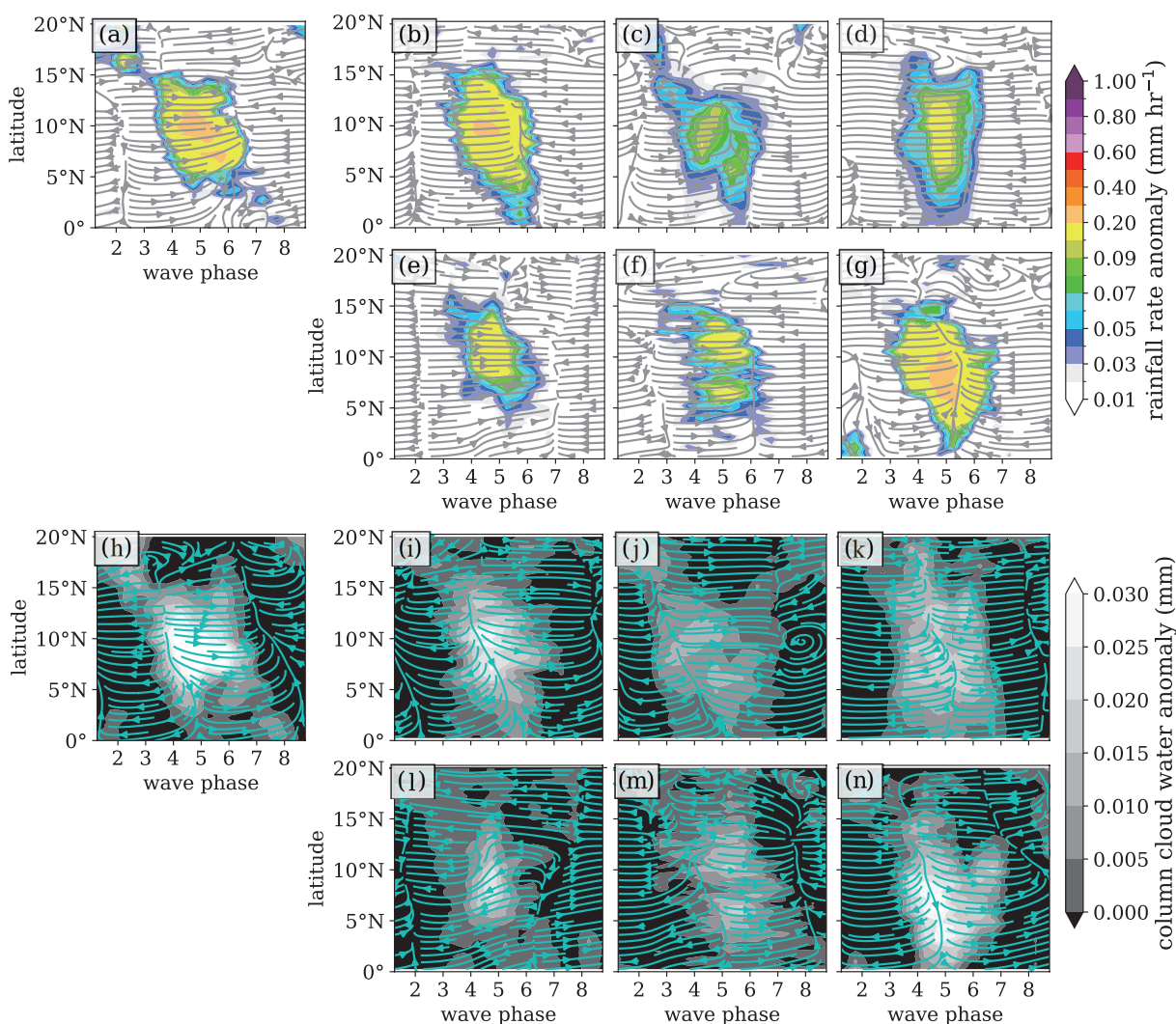
Fig. 5.   Wave phase–latitude composites (horizontal cross sections) for Kelvin waves. The top two rows (a–g) show wave-induced rainfall rate anomalies (shading) and 850-hPa horizontal winds (streamlines). The bottom two rows (h–n) show column cloud water anomalies (shading) and 200-hPa horizontal winds (streamlines). Each panel corresponds to a different data source: (a) IMERG (rainfall) and ERA5 (winds); (h) ERA5 (cloud water and winds); and for the remaining simulations: (b, i) 3.75-km EXP, (c, j) 15-km PAR, (d, k) 120-km PAR, (e, l) 3.75-km PAR, (f, m) 15-km EXP, and (g, n) 15-km PAR-2. The x-axis represents wave phase, where phase 5 is the wave crest (active convection) and phase 1 is the trough (suppressed convection).

plitudes and degrees of realism. A few general patterns become quickly apparent: First, the models reproduce the vertical motion field with greater fidelity than the more complex moisture and temperature fields, where model-to-observation differences are more pronounced. Second, regarding amplitude, the 3.75-km EXP run (Figs. 6b, i, p) and 15-km PAR-2 run (Figs. 6g, n, u) consistently produce the strongest anomalies and are stronger than ERA5 across all variables. For

the temperature anomaly, all simulations appear to overestimate the magnitude compared to the reanalysis data.

The most significant factor determining a simulation's structural realism is its treatment of convection. Specifically, runs using explicit convection tend to better capture observed tilts and phase relationships, whereas those using parameterized convection often produce anomalies that are too upright and improperly
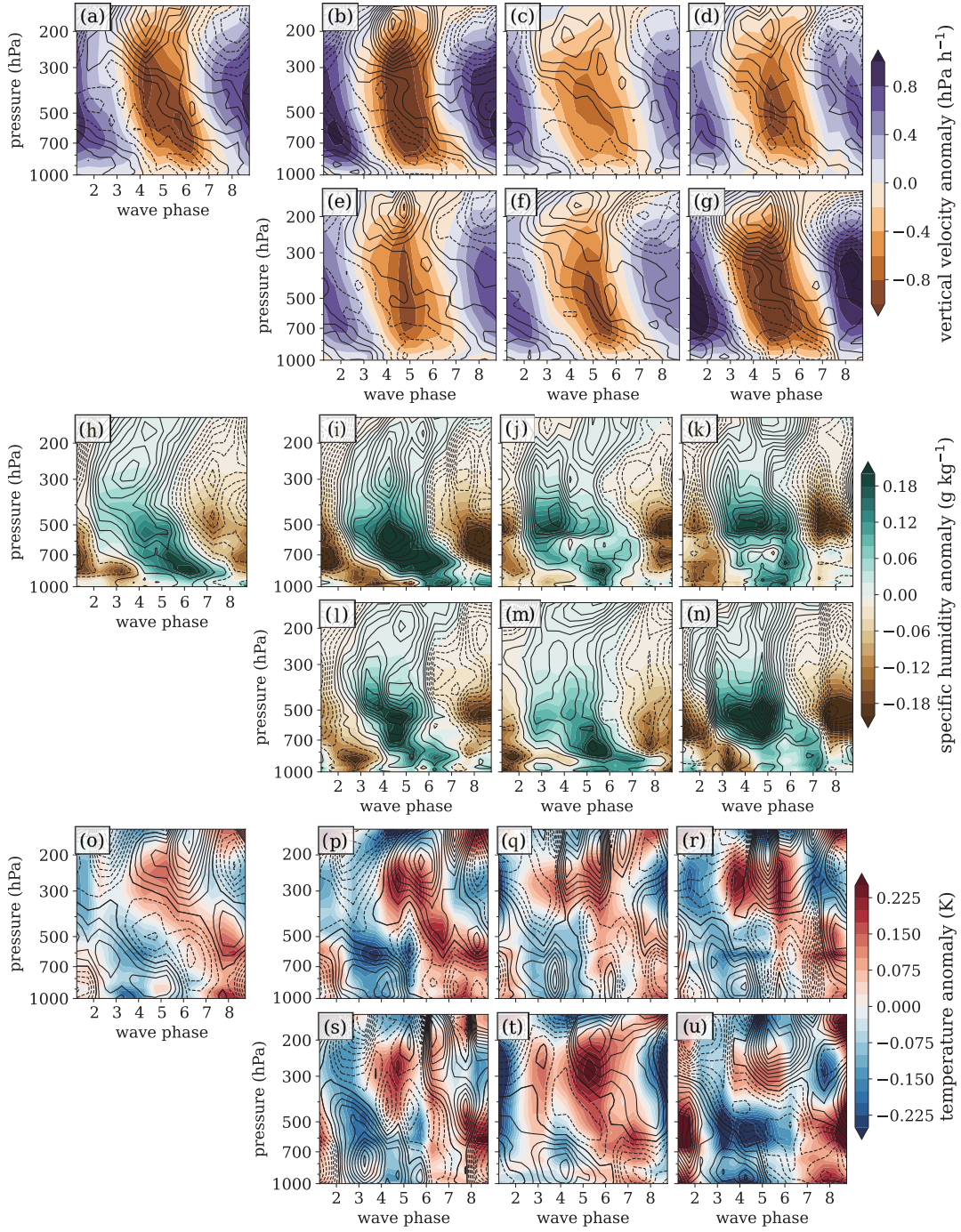
Fig. 6.   Wave phase–height composites (vertical cross sections) for Kelvin waves. The top two rows (a–g) show anomalous vertical velocity (color shading, intervals of 0.6 hPa h^{-1}) and divergence (contours, intervals of 3.0 × 10^{-7} s^{-1}). The middle two rows show anomalous water vapor mixing ratio (color shading, intervals of 0.05 g kg^{-1}) and relative humidity (contours, intervals of 2 %). The bottom two rows show anomalous temperature (color shading, intervals of 0.1 K) and apparent heat source (contours, intervals of 0.9 K day^{-1}). Each column corresponds to a different data source: (a, h, o) ERA5; (b, i, p) 3.75-km EXP; (c, j, q) 15-km PAR; (d, k, r) 120-km PAR; (e, l, s) 3.75-km PAR; (f, m, t) 15-km EXP; and (g, n, u) 15-km PAR-2. Wave phase 5 corresponds to the convectively active crest, while phase 1 represents the suppressed trough.
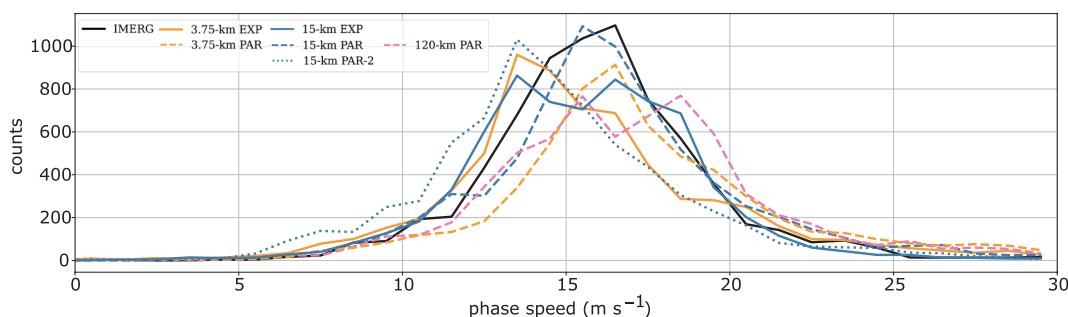
Fig. 7.   Distribution of Kelvin wave phase speeds. IMERG "observations" are shown in black. Solid lines represent simulations where the overwhelming amount of precipitation is explicit, dashed lines indicate runs where most of the precipitation is parameterized, and dotted lines correspond to the 15-km PAR-2 run (which has nearly an equal split between explicit and parameterized precipitation). The 3.75-km runs are shown in orange, the 15-km runs in dark blue, and the 120-km run in pink.

phased. Noteworthy biases in the runs with parameterized convection include:

- The ascent core is consistently too vertically upright, lacking the realistic westward tilt produced by explicit convection (Figs. 6c–e). This is particularly evident when comparing the brown-shaded region within the innermost ascent contour between the 3.75-km PAR and 15-km EXP runs (Figs. 6e, f).
- Moisture anomalies are also too upright and lack the observed westward tilt, a bias that is especially prominent in the 120-km PAR run (Fig. 6k).
- The mixing ratio anomaly peaks at an erroneously high altitude in the troposphere (500 hPa) in all simulations that use an active parameterization scheme, including the 15-km PAR-2 run (Figs. 6j–l, n).
- The vertical separation between mixing ratio and humidity peaks is lost, as they become vertically co-located at the same altitude (Figs. 6j–l, n).
- Failure to capture the quadrature relationship where heating leads temperature, and the heating fields themselves are too vertically upright (Figs. 6j–l, n).
- Some configurations produce exaggerated and unrealistic features, such as the strong cold anomaly in the 15-km PAR-2 run extending from the surface to 400 hPa (Fig. 6u).

c.   Phase speed

The analysis of phase speed reveals notable discrepancies among the simulations (Fig. 7). The observed distribution, derived from reanalysis, is bell-shaped and peaks near 17 m s^{-1}. Somewhat unexpectedly, the EXP runs do not outperform the PAR runs in this regard. Rather, the 15-km PAR run most closely replicates the observed distribution, while the 3.75-km PAR run also peaks at the correct speed but underes-

timates the amplitude. The simulations with explicit convection (solid lines) exhibit a clear slow bias. For instance, the 3.75-km EXP run—which otherwise performs best in capturing wave structure and precipitation—peaks around 13 m s^{-1}, a few m s^{-1} slower than observed. The 15-km EXP run peaks at a similar speed but exhibits a broader distribution overall. A slow bias is also present in the 15-km PAR-2 run, which again behaves more like the explicit-convection simulations than the other PAR runs.

4.2   (n = 1) Inertio-gravity waves
a.   Horizontal structure

Compared to Kelvin waves, the observed rain and cloud anomalies for inertio-gravity waves are somewhat weaker and less expansive (Figs. 8a, h). The associated wind field shows a low-level confluence axis centered within the rain shield, separating westerlies to its west from easterlies to its east (Fig. 8a). This flow pattern reverses at upper levels, where a diffluence axis over the cloud shield is flanked by easterlies to the west and westerlies to the east (Fig. 8h).

A clear performance hierarchy emerges among the simulations, with significant variations in both the amplitude of the anomalies and the realism of the wind-rainfall phasing. Regarding amplitude, the strength of the simulated rain and cloud anomalies is consistent with the rain anomalies in Fig. 4: The 3.75-km EXP and 15-km PAR-2 runs produce the strongest and most realistic precipitation signals (Figs. 8b, i, g, n), the 15-km EXP run follows at some distance (Figs. 8f, m), while the 3.75-km PAR, 15-km PAR, and 120-km PAR runs substantially underestimate the rainfall and cloud anomaly strength (Figs. 8c–e, j–l).

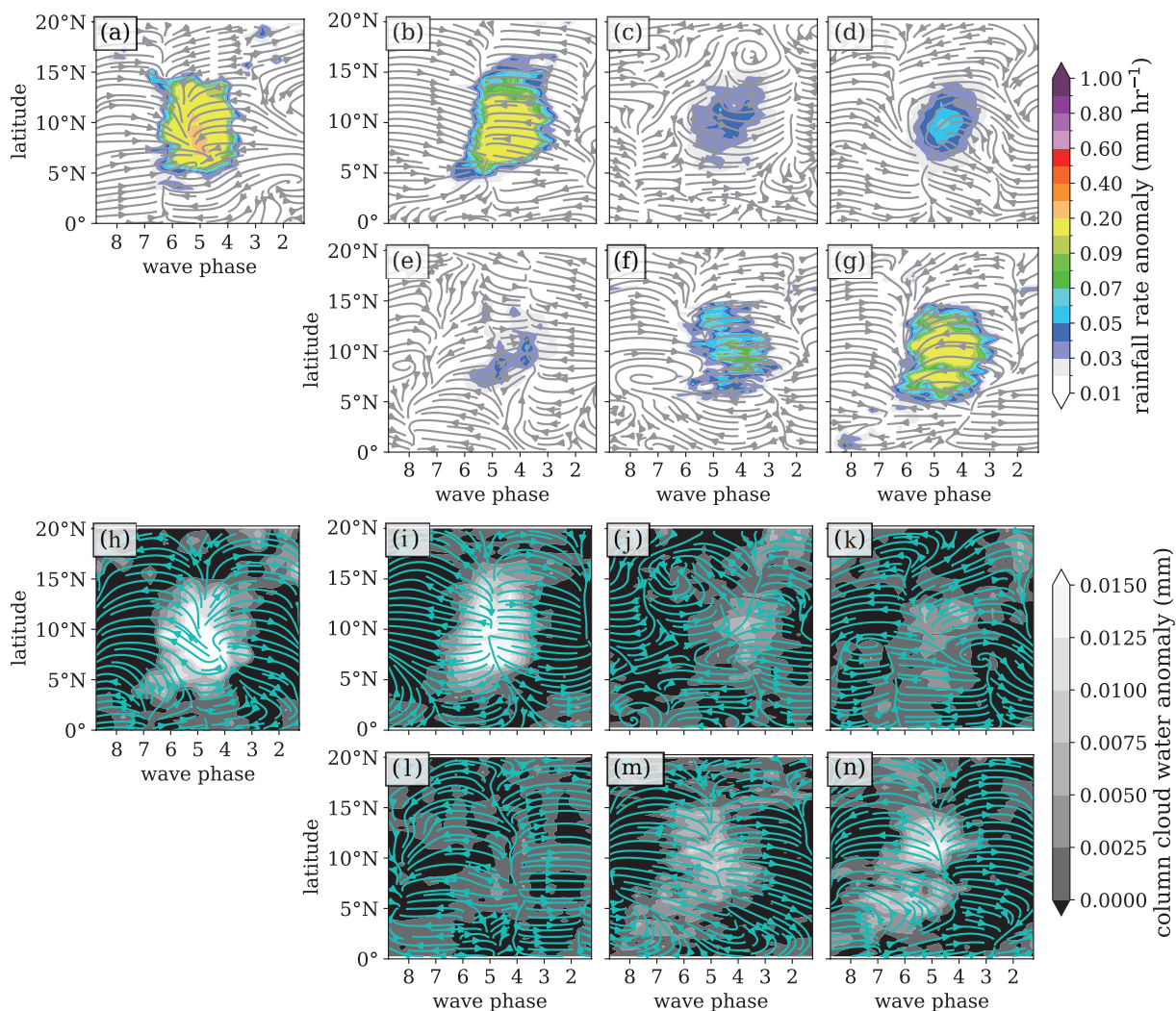None of the simulations correctly capture the low-

Fig. 8.   Same as Fig. 5, but for ($n = 1$) inertio-gravity waves.

level wind-rainfall phasing. Even the strongest runs—the 3.75-km EXP and 15-km PAR-2—misplace the low-level confluence axis too far to the west (Figs. 8b, g). However, those simulations at least capture the essential wind patterns, whereas runs relying on parameterized rainfall exhibit disorganized and unrealistic low-level flow. The upper-level flow is simulated more realistically, with the 3.75-km EXP, 15-km EXP, and 15-km PAR-2 runs successfully capturing the observed winds and diffluence zone within the cloud mass (Figs. 8i, m, n). It appears that the superior performance of these simulations in the upper levels directly correlates with their more realistic rain and cloud fields.

b. Vertical structure

In ERA5, inertio-gravity waves feature a coherent, eastward-tilted structure with complex phase relationships between the dynamic, moisture, and thermal fields (Figs. 9a, h, o). The wave's vertical motion forms an eastward-leaning "tower" of ascent that peaks between 500 hPa and 300 hPa (Fig. 9a). This ascent is preceded by a narrow, tilted band of low-level convergence. Upper-level divergence is maximized directly above the ascent core (phase 5, 200 hPa).

The moisture field is intricate, characterized by a "dry-over-moist" pattern west of the wave crest and a "moist-over-dry" pattern to its east (Fig. 9h). The low-level mixing ratio anomaly ahead of the wave (peaking in phase 7 at 800 hPa) is vertically distinct
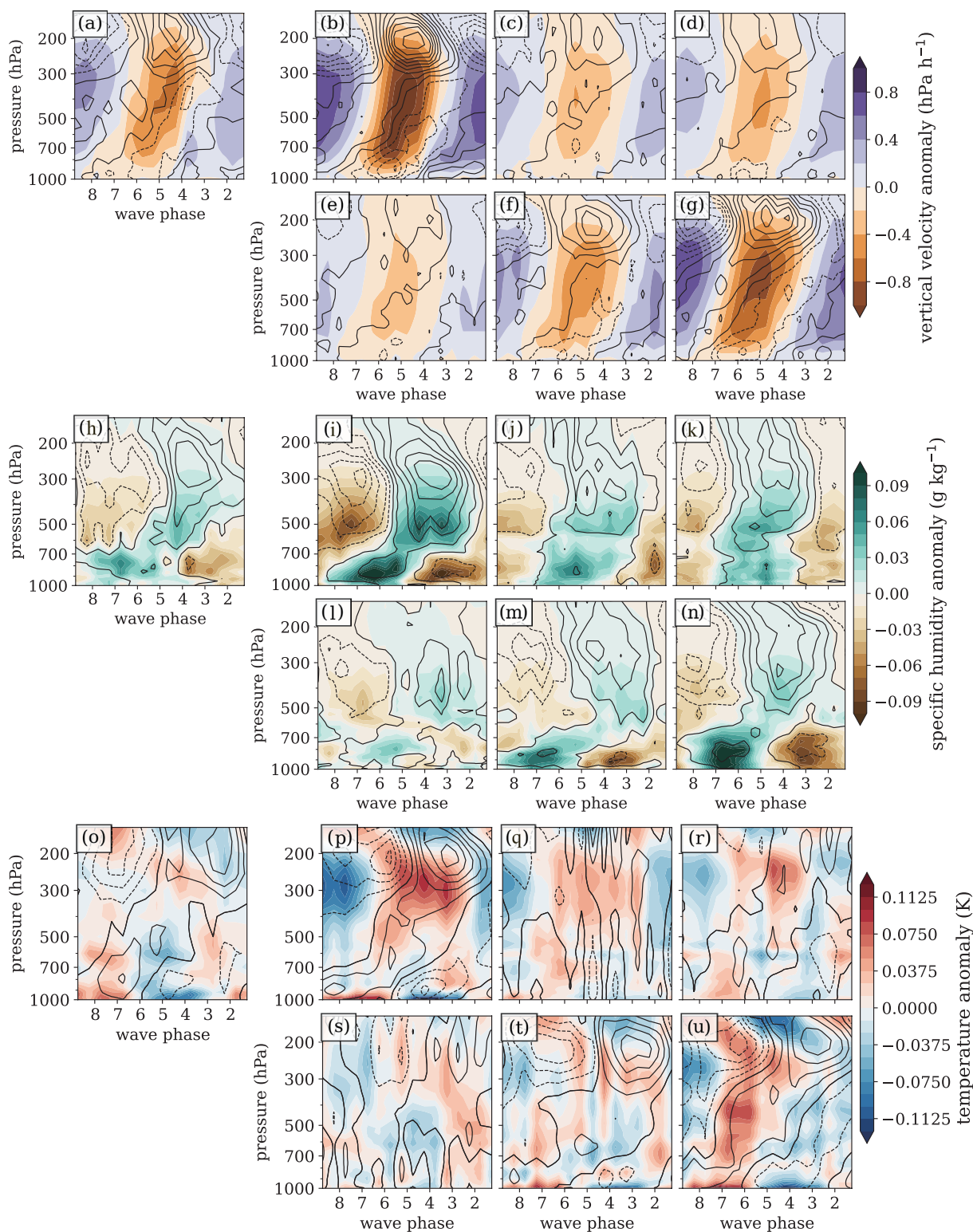
Fig. 9.   Same as Fig. 6, but for ($n = 1$) inertio-gravity waves.

from a separate mid-level mixing ratio anomaly behind it (peaking in phase 4 at 500 hPa). As with other wave types, relative humidity anomalies are strongest in the upper levels, while mixing ratio anomalies are most pronounced in the lower and mid-troposphere.

The temperature anomaly pattern is faint and less coherent than the moisture pattern (Fig. 9o). A dipole is nevertheless apparent in the lower levels, composed of a warm anomaly far ahead of the wave crest (peaking in phase 7) and a subsequent cold anomaly trailing behind it (peaking around phases 4 and 5). While the upper-level thermal pattern is difficult to discern, it appears to be reversed. The associated field of anomalous heating is more organized, forming a tilted ribbon that stretches across the wave. This structure rises from a peak near the surface in phase 7 and culminates in an upper-tropospheric heating maximum in phase 2 (at 200 hPa). This upper-level heating, paired with significant cooling at the same altitude ahead of the crest (phase 7), forms another distinct dipole.

With respect ti simulations, a clear performance hierarchy emerges that is again closely tied to the treatment of convection. The group of simulations that comprises the two explicit convection (EXP) runs and the 15-km PAR-2 run consistently provides a more realistic depiction of the wave's dynamic and thermodynamic structure. In contrast, the PAR simulations exhibit significant and recurring deficiencies. The following analysis explores this distinction across key fields:

- Dynamics (Vertical Motion): The amplitudes vary significantly. The 3.75-km EXP run produces the strongest signal (2−3 times that of ERA5; Fig. 9b), followed by the 15-km PAR-2 (Fig. 9g) and 15-km EXP runs (Fig. 9f). In contrast, the PAR runs produce much weaker ascent (Figs. 9c−e). Notably, and unlike in the Kelvin wave case, the degree of vertical tilt is not strongly dependent on the treatment of convection.
- Moisture: A similar performance hierarchy emerges for the moisture field. The 3.75-km EXP run provides the closest match to the observed structure, albeit with a significantly stronger amplitude (Fig. 9i). In general, the explicit convection runs (Fig. 9i, m) and the 15-km PAR-2 run (Fig. 9n) better capture the complex moisture layering, although the PAR-2 run places too much emphasis on the lower-level moisture anomaly. The nominal PAR runs struggle, producing structures that are too vertically upright (Figs. 9j−l).
- Thermal Fields: For temperature and heating, the same group of models excels, though a definitive

hierarchy is more difficult to assess due to the noisier nature of the fields. The EXP runs and the 15-km PAR-2 run produce more coherent temperature anomalies in approximately the correct location (Figs. 9p, u, t), unlike the other PAR simulations (Figs. 9q−s). Crucially, only the EXP and PAR-2 runs are able to capture both the tilted heating ribbon and the characteristic upper-level dipole of cooling ahead and warming behind the wave crest (Figs. 9p, u, t).

c. Phase speed

The analysis of inertio-gravity wave phase speeds reveals a similar paradox to that of Kelvin waves, though with an even more pronounced bias in the 3.75-km EXP run (Fig. 10). While observations show a broad phase speed distribution for these waves, with a peak near -24 m s^{-1}, the 3.75-km EXP run is a stark outlier, with its entire distribution shifted significantly toward slower (i.e., less negative) speeds. All other simulations align more closely with the observed distribution. However, it is important to note that the the simulations with the most accurate propagation speeds are precisely those that exhibit weak wave amplitudes and unrealistic structures.

4.3 Easterly waves
a. Horizontal structure

Of the three wave types, easterly waves produce the most intense rain and cloud anomalies (Figs. 11a, h). Their circulation is characterized by a pair of low-level cyclonic and anticyclonic gyres; the cyclonic gyre dominates the active phase of the wave, while an anticyclonic gyre prevails during the suppressed phase (Fig. 11a). In the upper levels, the flow is predominantly zonal and features a distinct diffluent zone in phase 5 (Fig. 11h). This diffluence, which is located slightly west of the center of the cloud shield zone, separates easterly winds to its west from westerly winds to its east.

The simulations generally reproduce the observed patterns of rain, clouds, and the characteristic gyres (Figs. 11b−g, i−n). Both the inter-model spread and the deviation from observations are smaller for this wave type than for inertio-gravity waves. Even so, anomaly magnitudes still vary, with a familiar pattern: the 3.75-km EXP and 15-km PAR-2 runs produce the strongest anomalies (Figs. 11b, g, i, n), with the signal in the PAR-2 run being notably distorted. The PAR runs tend to be weaker, exhibiting less robust circulations and some misalignment between the upper-level flow and the cloud shield (Figs. 11c−e, j−l).
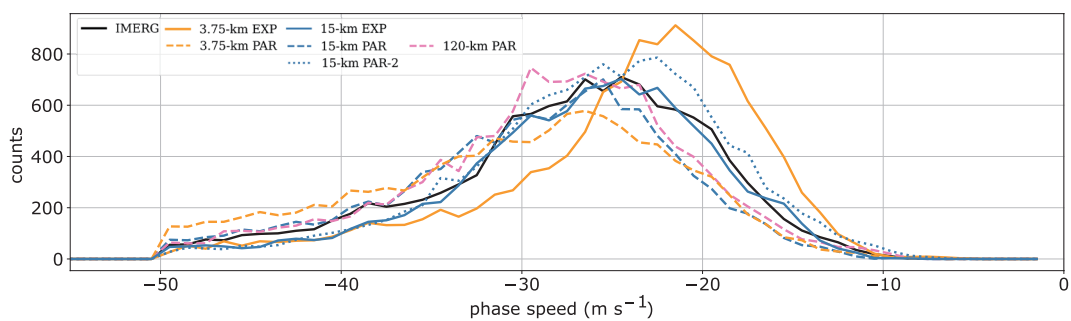
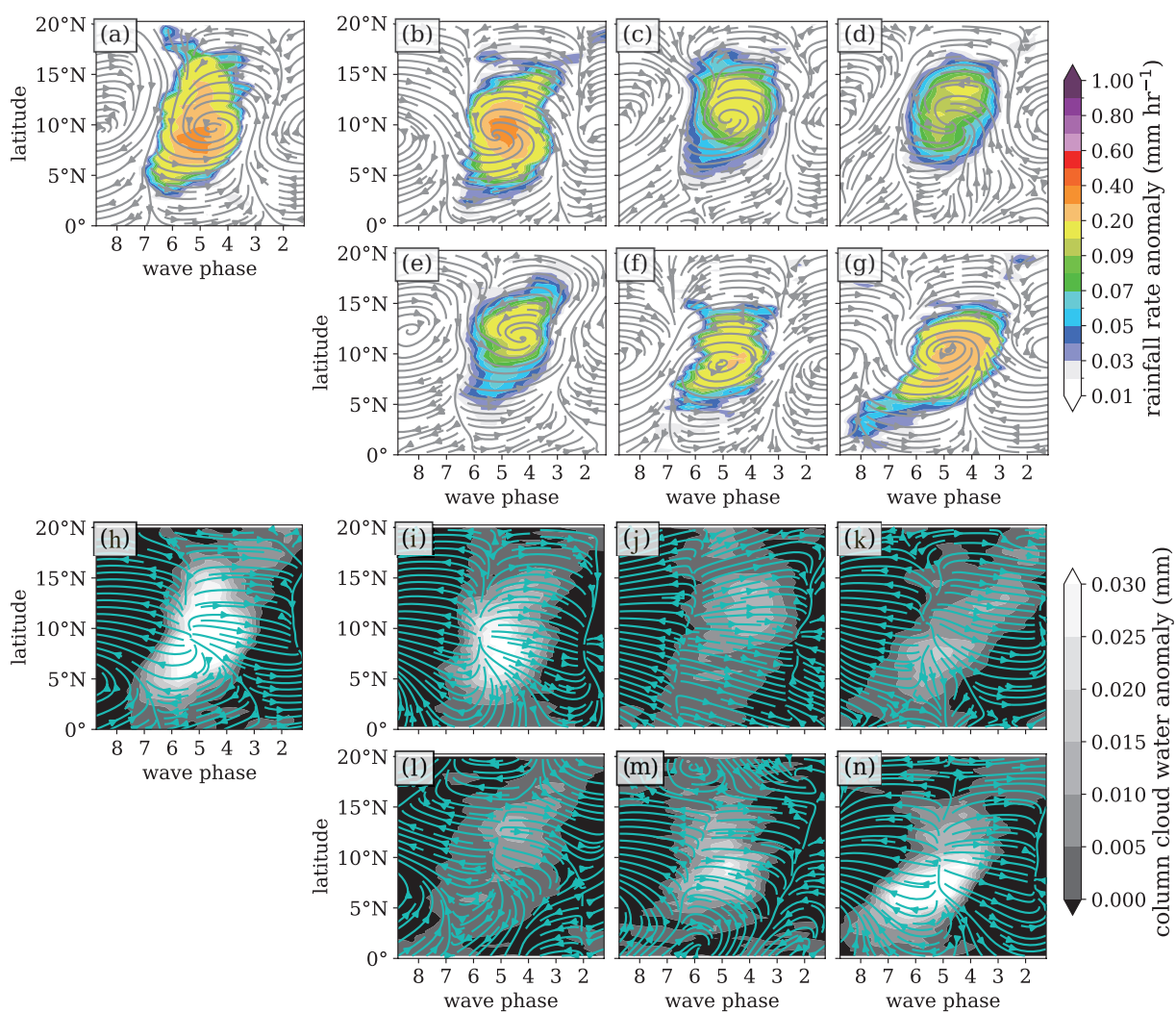Fig. 10.　Same as Fig. 7, but for inertio-gravity waves.

Fig. 11.　Same as Fig. 5, but for easterly waves.

b.   Vertical structure

In the ERA5 reanalysis, easterly waves exhibit a vertically deep, largely upright structure across their dynamic and moisture fields, accompanied by a complex quadrupole temperature pattern (Figs. 12a, h, o). The wave's dynamics are defined by a coherent tower of ascent with a slight eastward tilt in the lower troposphere, which aligns with a pronounced region of low-level convergence maximized near the wave crest (Fig. 12a). Upper-level divergence peaks near 200 hPa directly above the low-level convergence maximum.

The associated moisture field is organized in a subtle boomerang-like shape, with the deepest anomalous moisture centered just west of the wave crest (Fig. 12h). This structure has two distinct maxima: the mixing ratio anomaly peaks lower in the atmosphere, around 600 hPa, while the relative humidity anomaly reaches its maximum higher up, near 300 hPa. The thermal field is even more complex, defined by a quadrupole pattern that transitions from a "cold-over-warm" anomaly west of wave phase 6 to an opposing "warm-over-cold" anomaly behind it (Fig. 12o). This lower tropospheric thermal structure is coupled with a distinct dipole in diabatic heating in the upper troposphere, where anomalous cooling precedes wave phase 6 and strong warming follows it.

The primary distinction between simulations is once again tied to the treatment of convection. In general, runs with explicit convection and the 15-km PAR-2 run produce higher-amplitude patterns and more strongly tilted structures in their dynamic and moisture fields.

Key detailed findings include:

- **Dynamics:** The 3.75-km EXP and 15-km PAR-2 runs produce the strongest vertical motion, with amplitudes exceeding ERA5 (Figs. 12b, g). The PAR runs are considerably weaker (Figs. 12c−e), while the 15-km EXP run is intermediate in strength (Fig. 12f). A structural difference is that explicit convection runs show a more pronounced eastward tilt, whereas parameterized runs are more vertically upright.
- **Moisture:** The EXP (Figs. 12i, m) and 15-km PAR-2 (Fig. 12n) runs display a more pronounced (perhaps excessive) vertical tilt. In contrast, the other parameterized runs produce a more upright structure but show a weaker vertical separation between mixing ratio and relative humidity peaks (Figs. 12j−l). The 15-km and 120-km PAR runs also exhibit an unrealistic striation near 600 hPa, likely related to the model's melting layer physics (Figs. 12j, k).

- **Thermal Fields:** The EXP and 15-km PAR-2 runs produce stronger anomalies and exhibit a complex, tilted boomerang structure in the lower troposphere that is absent or only faintly suggested in the ERA5 reanalysis (Figs. 12p, t, u). In contrast, the PAR simulations, while weaker, align more closely with the reanalysis data (Figs. 12q−s).

c.   Phase speed

The trade-off between structural fidelity and propagation speed persists in the analysis of easterly waves (Fig. 13), although it is less pronounced than for inertio-gravity waves. The observed distribution is bell-shaped with a leftward skew, peaking near −8 m s^{-1} to −9 m s^{-1}. Consistent with other wave types, the 3.75-km EXP run underperforms in this metric, producing a distribution shifted toward faster speeds around −11 m s^{-1} and featuring an irregular shape. The 15-km EXP run exhibits a similar fast bias. In contrast, the traditionally parameterized simulations better capture the observed peak speed and, overall, exhibit more realistic distribution shapes. Contrary to the previous phase speed analyses, the 15-km PAR-2 run's bias is the inverse of the EXP simulations: here it displays a rightward shift toward slower propagation speeds.

5.   Discussion

A primary conclusion from this study is that high-resolution simulations with explicit convection generally yield the most realistic tropical wave structures. However, our findings also reveal critical nuances that preclude a simple "explicit convection is always better" narrative. For example, the superior performance of the 3.75-km EXP run compared to the 15-km EXP run suggests that explicit convection is only effective at truly convection-permitting resolutions. This finding contrasts with other studies using the NICAM model, which reported good results at 14-km resolution without a convection scheme (e.g., Kodama et al. 2015; Goto et al. 2020; Seiki and Ohno 2023).

To investigate whether the superior structural realism of the 3.75-km EXP run reflects a deeper physical consistency, we inferred rainfall from the waves' circulation and moisture fields. We hypothesized that the most realistic three-dimensional wave structures would yield the most accurate rainfall estimates. Using vertical moisture flux following Doswell (1996), we estimate rainfall rate (f) as

$$f = \overline{\epsilon w_+ q_v}. \tag{1}$$

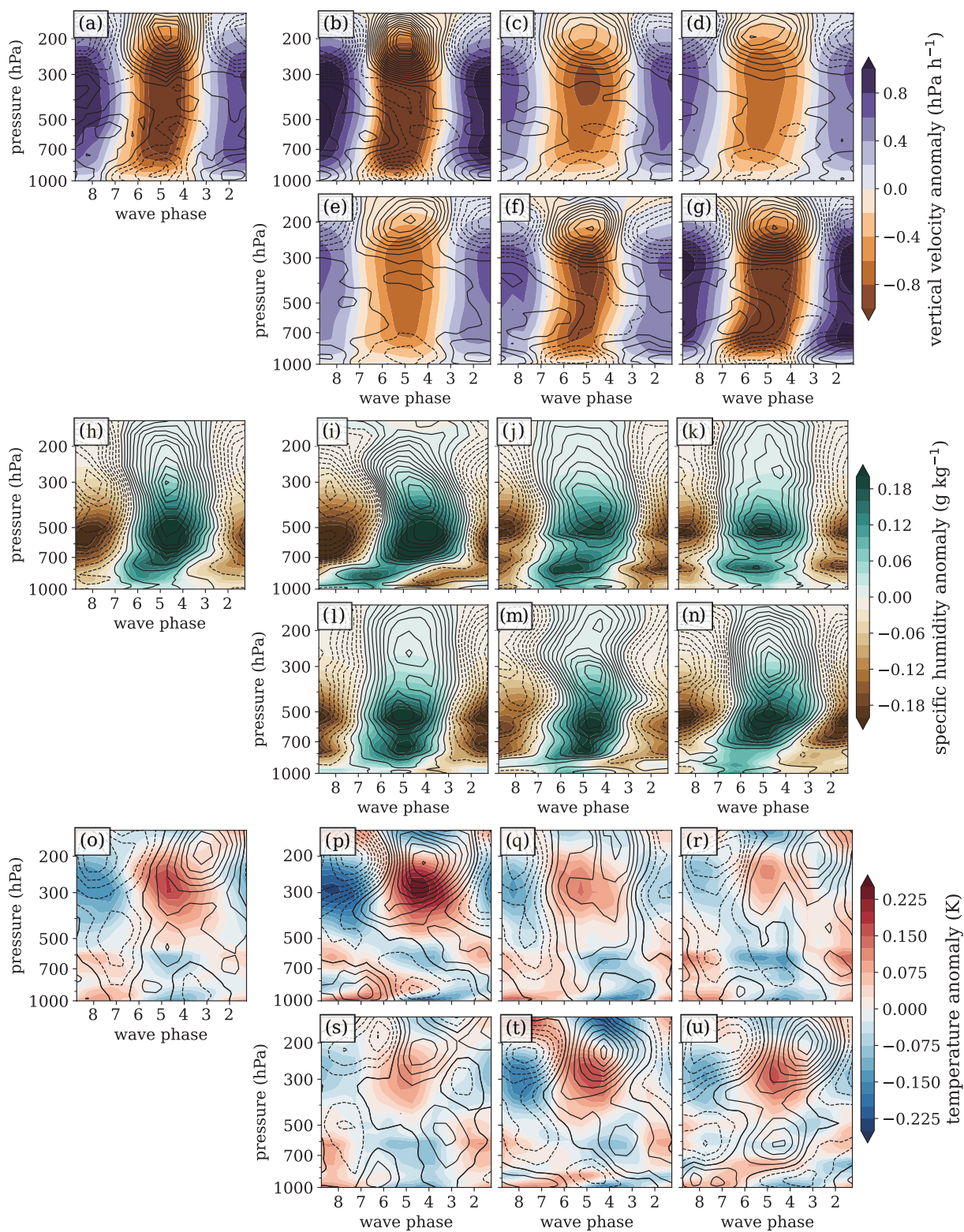Here, w_+ denotes the upward vertical velocity, q_v

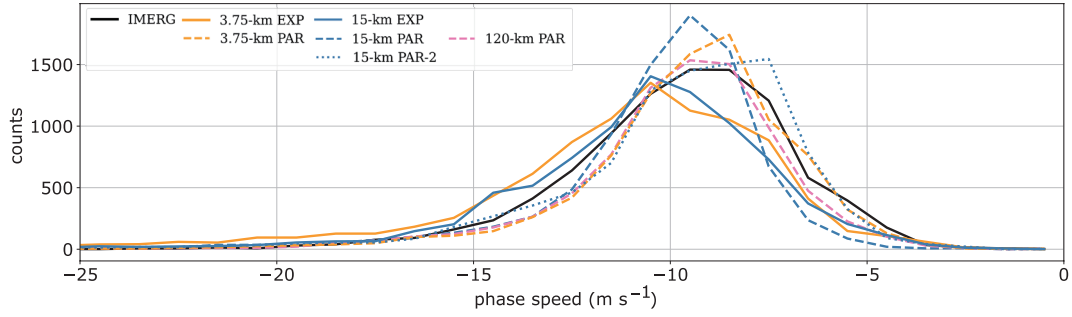Fig. 12. Same as Fig. 6, but for easterly waves.

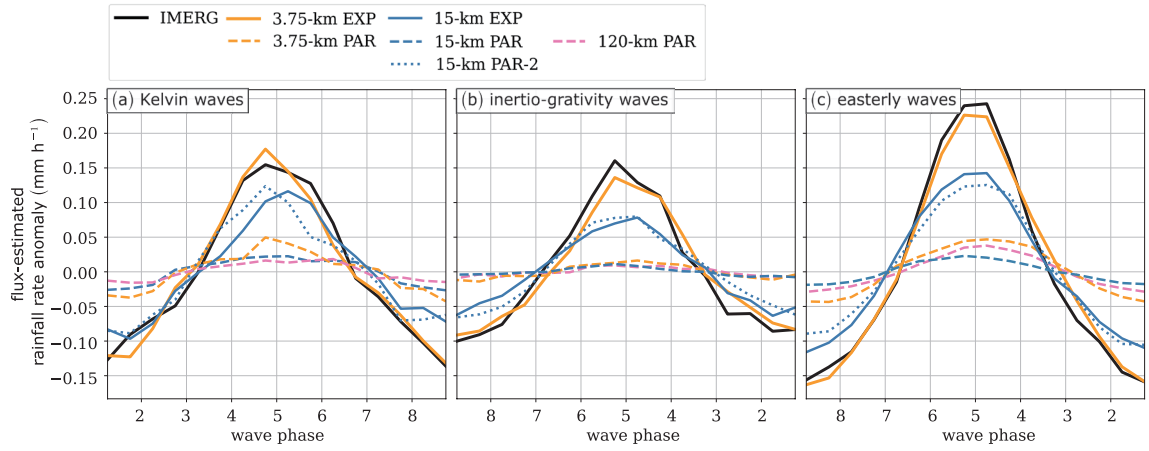Fig. 13.   Same as Fig. 7, but for easterly waves.

Fig. 14.   Wave phase–latitude composites of precipitation rates estimated from vertical water vapor flux. The layout and data sources are identical to those in Fig. 4. This "derived" precipitation is shown to assess the physical consistency of the rainfall produced in each simulation.

the water vapor mixing ratio, and ϵ the precipitation efficiency, assumed constant at 0.9 for simplicity. The overbar denotes a vertical average over the $700-1000$ hPa layer (this is where most of the moisture resides). The resulting values are then averaged over the $5-15°N$ latitude band.

The analysis affirms the hypothesis and reveals the 3.75-km EXP run's unique physical consistency (Fig. 14). This is the only simulation that produces flux-derived rainfall that both matches IMERG and successfully "recovers" its own native precipitation field (cf. Figs. 14, 4). This success underscores a critical point: accurately capturing wave structure is crucial not merely for simulating rainfall, but for ensuring it emerges organically from the underlying physics.

Overall, our results extend and reinforce findings by Judt and Rios-Berrios (2021) and Rios-Berrios et al. (2023), confirming that realistic wave behavior hinges on resolving convection at high resolution. However,

the success in structural realism is tempered by a challenging trade-off: an inverse relationship between structural fidelity and propagation speed accuracy. This may occur because the physical mechanisms governing wave structure are largely distinct from those controlling phase speed. For instance, improvements in structure via explicit convection might alter wave–mean flow interactions in ways that bias the phase speed. Alternatively, the discrepancy may not reflect a physical phenomenon but could instead be a methodological artifact stemming from our phase speed calculations. Resolving this tension requires further investigation into wave energy budgets, convection–wave feedbacks, and interactions with the background flow.

Beyond this specific puzzle, the broader landscape of atmospheric modeling remains nuanced; operational models with parameterized convection continue to improve (Dias et al. 2023), while convection-resolving

models still face their own notable shortcomings (e.g., Lawton et al. 2024).

Several limitations of this study also warrant mention:

- All simulations were conducted with a single model, limiting the generalizability of the conclusions. Broader insights will require future model intercomparison studies.
- Computational constraints limited the simulations' duration, reducing the robustness of the statistics.
- We relied on the Wheeler–Kiladis method for wave detection. Alternative techniques may yield different insights (Knippertz et al. 2022; Jung and Knippertz 2023).
- While our results suggest that global km-scale models may improve forecasts in the tropics, we do not directly evaluate forecast skill, and the observed biases in wave propagation speed raise questions about how structural improvements translate to predictive performance.

6. Summary and conclusions

The present study provides a systematic evaluation of how horizontal resolution and convection treatment affect the simulation of tropical waves in the global non-hydrostatic MPAS-A model. We analyzed six 40-day long simulations, spanning resolutions from 120 km to 3.75 km and convection treatment from explicit to parameterized. By comparing composite structures of Kelvin, $n = 1$ inertio-gravity, and easterly waves against observations and reanalysis, we identified the key factors that yield more realistic wave behavior.

Our findings reveal that explicitly resolving convection provides a decisive advantage in capturing realistic wave structures, with the high-resolution 3.75-km EXP run consistently setting the benchmark for performance. This superiority stems from its ability to reproduce the three-dimensional coupling between rainfall, circulation, and thermodynamics. The key takeaways are:

- A Complex Interplay of Resolution, Convection Treatment, and Model Errors: While the 3.75-km explicit run delivered the most realistic results and the traditionally parameterized simulations performed uniformly poorly, two additional 15-km simulations revealed a more nuanced trade-off. The 15-km explicit run produced less realistic wave structures than the 3.75-km explicit run and suffered from weak wave amplitude and a disorganized precipitation pattern. Conversely, the 15-km run with an alternative convection scheme yielded more coherent

wave-related rainfall and structure, yet exhibited a substantial overall wet bias. Thus, a truly realistic simulation required both high resolution and explicit convection, while moderate-resolution approaches force a choice between significant, competing errors.
- A Paradoxical Trade-Off in Phase Speed: A critical and unexpected finding was the inverse relationship between structural accuracy and propagation speed. While explicit convection runs excelled at representing wave structure, they struggled to reproduce observed propagation speeds. The 3.75-km explicit convection run, despite its structural realism, exhibited phase speed biases for all wave types. Conversely, parameterized simulations, despite their poor structures and weak amplitudes, showed better agreement with observed phase speeds.
- When the Physics Adds Up, the Model is More Realistic: The structural integrity of the 3.75-km explicit convection run reflects a deeper physical consistency. It was the only simulation where precipitation estimated from vertical moisture flux closely matched the model's direct rainfall output, confirming that its realistic structures produce rainfall for the right reasons.

In summary, our work confirms that high resolution and explicit convection are critical for capturing the intricate dynamics of tropical waves. However, we also reveal a fundamental trade-off between structural realism and propagation speed that should be addressed. Despite this hurdle, the gains in physical realism confirm that embracing global km-scale models is a promising path toward the next generation of weather and climate prediction.

References

Bartana, H., C. I. Garfinkel, O. Shamir, and J. Rao, 2023: Projected future changes in equatorial wave spectrum in CMIP6. *Climate Dyn.*, **60**, 3277–3289.

Bengtsson, L., J. Dias, M. Gehne, P. Bechtold, J. Whitaker, J.-W. Bao, L. Magnusson, S. Michelson, P. Pegion, S. Tulich, and G. N. Kiladis, 2019: Convectively coupled equatorial wave simulations using the ECMWF IFS and the NOAA GFS cumulus convection schemes in the NOAA GFS model. *Mon. Wea. Rev.*, **147**, 4005–4025.

Chien, M.-T., and D. Kim, 2023: Representation of the convectively coupled Kelvin waves in modern reanalysis products. *J. Atmos. Sci.*, **80**, 397–418.

Dias, J., M. Gehne, G. N. Kiladis, N. Sakaeda, P. Bechtold, and T. Haiden, 2018: Equatorial waves and the skill of NCEP and ECMWF numerical weather prediction systems. *Mon. Wea. Rev.*, **146**, 1763–1784.

Dias, J., M. Gehne, G. N. Kiladis, and L. Magnusson, 2023: The role of convectively coupled equatorial waves in sub-seasonal predictions. *Geophys. Res. Lett.*, **50**, e2023GL106198, doi:10.1029/2023GL106198.

Doswell, III, C. A., H. E. Brooks, and R. A. Maddox, 1996: Flash flood forecasting: An ingredients-based methodology. *Wea. Forecasting*, **11**, 560–581.

Frierson, D. M. W., D. Kim, I.-S. Kang, M.-I. Lee, and J. Lin, 2011: Structure of AGCM-simulated convectively coupled Kelvin waves and sensitivity to convective parameterization. *J. Atmos. Sci.*, **68**, 26–45.

Fudeyasu, H., Y. Wang, M. Satoh, T. Nasuno, H. Miura, and W. Yanase, 2008: Global cloud-system-resolving model NICAM successfully simulated the lifecycles of two real tropical cyclones. *Geophys. Res. Lett.*, **35**, L22808, doi:10.1029/2008GL036003.

Goto, D., Y. Sato, H. Yashiro, K. Suzuki, E. Oikawa, R. Kudo, T. M. Nagao, and T. Nakajima, 2020: Global aerosol simulations using NICAM.16 on a 14 km grid spacing for a climate study: Improved and remaining issues relative to a lower-resolution model. *Geosci. Model Dev.*, **13**, 3731–3768.

Hersbach, H., B. Bell, P. Berrisford, S. Hirahara, A. Horányi, J. Muñoz-Sabater, J. Nicolas, C. Peubey, R. Radu, D. Schepers, A. Simmons, C. Soci, S. Abdalla, X. Abellan, G. Balsamo, P. Bechtold, G. Biavati, J. Bidlot, M. Bonavita, G. De Chiara, P. Dahlgren, D. Dee, M. Diamantakis, R. Dragani, J. Flemming, R. Forbes, M. Fuentes, A. Geer, L. Haimberger, S. Healy, R. J. Hogan, E. Hólm, M. Janisková, S. Keeley, P. Laloyaux, P. Lopez, C. Lupu, G. Radnoti, P. de Rosnay, I. Rozum, F. Vamborg, S. Villaume, and J.-N. Thépaut, 2020: The ERA5 global reanalysis. *Quart. J. Roy. Meteor. Soc.*, **146**, 1999–2049.

Huffman, G. J., D. T. Bolvin, D. Braithwaite, K.-L. Hsu, R. J. Joyce, C. Kidd, 714 E. J. Nelkin, S. Sorooshian, E. F. Stocker, J. Tan, D. B. Wolff, and P. Xie, 2020: Integrated multi-satellite retrievals for the global precipitation measurement (GPM) mission (IMERG). *Satellite Precipitation Measurement*. Levizzani, V., C. Kidd, D. B. Kirschbaum, C. D. Kummerow, K. Nakamura, and T. F. Turk (eds). Advances in Global Change Research, No. 67, Springer, Cham, 343–353.

Judt, F., and R. Rios-Berrios, 2021: Resolved convection improves the representation of equatorial waves and tropical rainfall variability in a global nonhydrostatic model. *Geophys. Res. Lett.*, **48**, e2021GL093265, doi: 10.1029/2021GL093265.

Judt, F., D. Klocke, R. Rios-Berrios, B. Vanniere, F. Ziemen, L. Auger, J. Biercamp, C. Bretherton, X. Chen, P. Düben, C. Hohenegger, M. Khairoutdinov, T. Kodama, L. Kornblueh, S.-J. Lin, M. Nakano, P. Neumann, W. Putman, N. Röber, M. Roberts, M. Satoh, R. Shibuya, B. Stevens, P. L. Vidale, N. Wedi, and L. Zhou, 2021: Tropical cyclones in global storm-resolving models. *J. Meteor. Soc. Japan*, **99**, 579–602.

Jung, H., and P. Knippertz, 2023: Link between the time-space behavior of rainfall and 3D dynamical structures of equatorial waves in global convection-permitting simulations. *Geophys. Res. Lett.*, **50**, e2022GL100973, doi:10.1029/2022GL100973.

Knippertz, P., M. Gehne, G. N. Kiladis, K. Kikuchi, A. Rasheeda Satheesh, P. E. Roundy, G.-Y. Yang, N. Žagar, J. Dias, A. H. Fink, J. Methven, A. Schlueter, F. Sielmann, and M. C. Wheeler, 2022: The intricacies of identifying equatorial waves. *Quart. J. Roy. Meteor. Soc.*, **148**, 2814–2852.

Kodama, C., Y. Yamada, A. T. Noda, K. Kikuchi, Y. Kajikawa, T. Nasuno, T. Tomita, T. Yamaura, H. G. Takahashi, M. Hara, Y. Kawatani, M. Satoh, and M. Sugi, 2015: A 20-year climatology of a NICAM AMIP-type simulation. *J. Meteor. Soc. Japan*, **93**, 393–424.

Lawton, Q. A., R. Rios-Berrios, S. J. Majumdar, R. Emerton, and L. Magnusson, 2024: The representation of convectively coupled Kelvin waves in simulations with modified wave amplitudes. *J. Adv. Model. Earth Syst.*, **16**, e2023MS004187, doi:10.1029/2023MS004187.

Lee, S.-H., S.-H. Park, M.-T. Chien, and D. Kim, 2025: Simulations of convectively coupled Kelvin waves (CCKWs) with three different cumulus parameterization schemes. *J. Geophys. Res.: Atmos.*, **130**, e2024JD042738, doi:10.1029/2024JD042738.

Lin, J.-L., G. N. Kiladis, B. E. Mapes, K. M. Weickmann, K. R. Sperber, W. Lin, M. C. Wheeler, S. D. Schubert, A. Del Genio, L. J. Donner, S. Emori, J.-F. Gueremy, F. Hourdin, P. J. Rasch, E. Roeckner, and J. F. Scinocca, 2006: Tropical intraseasonal variability in 14 IPCC AR4 climate models. Part I: Convective signals. *J. Climate*, **19**, 2665–2690.

Lin, J.-L., B. E. Mapes, K. M. Weickmann, G. N. Kiladis, S. D. Schubert, M. J. Suarez, J. T. Bacmeister, and M.-I. Lee, 2008: North American monsoon and convectively coupled equatorial waves simulated by IPCC AR4

coupled GCMs. *J. Climate*, **21**, 2919–2937.

Miura, H., M. Satoh, T. Nasuno, A. T. Noda, and K. Oouchi, 2007: A Madden-Julian oscillation event realistically simulated by a global cloud-resolving model. *Science*, **318**, 1763–1765.

Miyakawa, T., M. Satoh, H. Miura, H. Tomita, H. Yashiro, A. T. Noda, Y. Yamada, C. Kodama, M. Kimoto, and K. Yoneyama, 2014: Madden-Julian Oscillation prediction skill of a new-generation global model demonstrated using a supercomputer. *Nat. Commun.*, **5**, 3769, doi:10.1038/ncomms4769.

Nakajima, K., Y. Yamada, Y. O. Takahashi, M. Ishiwatari, W. Ohfuchi, and Y.-Y. Hayashi, 2013: The variety of spontaneously generated tropical precipitation patterns found in APE results. *J. Meteor. Soc. Japan*, **91A**, 91–141.

Rios-Berrios, R., F. Judt, G. Bryan, B. Medeiros, and W. Wang, 2023: Three-dimensional structure of convectively coupled equatorial waves in aquaplanet experiments with resolved or parameterized convection. *J. Climate*, **36**, 2895–2915.

Satoh, M., T. Matsuno, H. Tomita, H. Miura, T. Nasuno, and S. Iga, 2008: Nonhydrostatic icosahedral atmospheric model (NICAM) for global cloud resolving simulations. *J. Comput. Phys.*, **227**, 3486–3514.

Schulzweida, U., 2023: CDO user guide. Technical report, Zenodo.

Seiki, T., and T. Ohno, 2023: Improvements of the double-moment bulk cloud microphysics scheme in the non-hydrostatic icosahedral atmospheric model (NICAM). *J. Atmos. Sci.*, **80**, 111–127.

Skamarock, W. C., J. B. Klemp, M. G. Duda, L. D. Fowler, S.-H. Park, and T. D. Ringler, 2012: A multiscale nonhydrostatic atmospheric model using centroidal Voronoi tesselations and C-grid staggering. *Mon. Wea. Rev.*, **140**, 3090–3105.

Stephens, G. L., T. L'Ecuyer, R. Forbes, A. Gettelmen, J.-C. Golaz, A. Bodas-Salcedo, K. Suzuki, P. Gabriel, and J. Haynes, 2010: Dreary state of precipitation in global models. *J. Geophys. Res.*, **115**, D24211, doi:10.1029/2010JD014532.

Stevens, B., M. Satoh, L. Auger, J. Biercamp, C. S. Bretherton, X. Chen, P. Düben, F. Judt, M. Khairoutdinov, D. Klocke, C. Kodama, L. Kornblueh, S.-J. Lin, P. Neumann, W. M. Putman, N. Röber, R. Shibuya, B. Vanniere, P. L. Vidale, N. Wedi, and L. Zhou, 2019: DYAMOND: The DYnamics of the atmospheric general circulation modeled on non-hydrostatic domains. *Prog. Earth Planet. Sci.*, **6**, 61, doi:10.1186/s40645-019-0304-z

Straub, K. H., P. T. Haertel, and G. N. Kiladis, 2010: An analysis of convectively coupled Kelvin waves in 20 WCRP CMIP3 global coupled climate models. *J. Climate*, **23**, 3031–3056.

Tomita, H., H. Miura, S. Iga, T. Nasuno, and M. Satoh, 2005: A global cloud-resolving simulation: Preliminary results from an aqua planet experiment. *Geophys. Res. Lett.*, **32**, L08805, doi:10.1029/2005GL022459.

Vogel, P., P. Knippertz, A. H. Fink, A. Schlueter, and T. Gneiting, 2018: Skill of global raw and postprocessed ensemble predictions of rainfall over northern tropical africa. *Wea. Forecasting*, **33**, 369–388.

Vogel, P., P. Knippertz, A. H. Fink, A. Schlueter, and T. Gneiting, 2020: Skill of global raw and postprocessed ensemble predictions of rainfall in the tropics. *Wea. Forecasting*, **35**, 2367–2385.

Wang, W., 2022: Forecasting convection with a "scale-aware" Tiedtke cumulus parameterization scheme at kilometer scales. *Wea. Forecasting*, **37**, 1491–1507.

Weber, N. J., C. F. Mass, and D. Kim, 2020: The impacts of horizontal grid spacing and cumulus parameterization on subseasonal prediction in a global convection-permitting model. *Mon. Wea. Rev.*, **148**, 4747–4765.

Weber, N. J., D. Kim, and C. F. Mass, 2021: Convection–Kelvin wave coupling in a global convection-permitting model. *J. Atmos. Sci.*, **78**, 1039–1055.

Wheeler, M., and G. N. Kiladis, 1999: Convectively coupled equatorial waves: Analysis of clouds and temperature in the wavenumber–frequency domain. *J. Atmos. Sci.*, **56**, 374–399.

Yanai, M., S. Esbensen, and J.-H. Chu, 1973: Determination of bulk properties of tropical cloud clusters from large-scale heat and moisture budgets. *J. Atmos. Sci.*, **30**, 611–627.

Zhang, C., and Y. Wang, 2017: Projected future changes of tropical cyclone activity over the western North and South Pacific in a 20-km-mesh regional climate model. *J. Climate*, **30**, 5923–5941.

Zhu, J., A. Kumar, and W. Wang, 2020: Dependence of MJO predictability on convective parameterizations. *J. Climate*, **33**, 4739–4750.